

Real-time equality-constrained hybrid state estimation in complex variables

Izudin Džafić^{a,*}, Rabih A. Jabr^b

^a International University of Sarajevo, Hrasnička cesta 15, 71210 Sarajevo, Bosnia and Herzegovina

^b Department of Electrical & Computer Engineering, American University of Beirut, P.O. Box 11-0236, Riad El-Solh, Beirut 1107 2020, Lebanon

ARTICLE INFO

Keywords:

Least squares approximation
Least squares methods
Optimization
Power system analysis computing
State estimation

ABSTRACT

The hybrid power system state estimation problem requires computing the state of the power network using data from both legacy and phasor measurements. Recent research has shown that the normal equations approach in complex variables is computationally advantageous, particularly in the presence of phasor measurement values, and that its software implementation is best suited to modern processors that employ single instruction multiple data (SIMD) processor extensions. The complex normal equations approach is however not ideal for handling zero injection measurements, as it requires their modeling as virtual measurements with high weights. This paper employs Wirtinger calculus for extending the complex normal equations approach to include equality constraints, and contrasts it with two previously published implementations: the normal equations approach in complex variables and the hybrid equality constrained state estimator in real variables. Numerical results are reported on transmission networks having up to 9241 nodes; they show that the complex variable equality constrained hybrid state estimator exhibits superior performance as compared to the above two techniques in terms of both computational time and accuracy. Moreover, the execution time on the largest network is less than 300 ms, which makes the proposed implementation commensurate with the requirements of real-time applications.

1. Introduction

The power system state estimation problem is most commonly formulated as a weighted least squares problem and solved via the normal equations (NE) approach; the main advantage of the NE approach is that it gives rise to a gain matrix that can be rapidly factorized using sparsity techniques. Nodes that have neither generation nor load are modeled as virtual zero complex power injection measurements, which are very useful to enhance the estimation accuracy. Zero injection measurements can be accounted for in the NE approach by assigning relatively much larger weights to them, but this can potentially cause ill-conditioning. It is now accepted that zero injections are best handled through formulating the estimation problem as an equality constrained optimization program, leading to methods such as the normal equations with equality constraints, Hatchel's augmented matrix method, and other hybrid forms and extensions [1–3].

In the current operational practice, state estimators are expected to employ measurements from both the supervisory control and data acquisition (SCADA) and the phasor measurement unit (PMU) systems. PMU measurements are increasingly being employed in power systems, with benefits in risk mitigation against cyber attacks [4], in Volt-Var control [5], and in transmission network state estimation [6,7].

Handling phasor current measurements in power grid state estimation can be accomplished using either noninvasive or direct techniques. The noninvasive methods have the distinct advantage of not requiring any update to the classical state estimator implementations that are based on SCADA measurements; they rather employ post processing techniques that improve the estimation outcome by fusing the SCADA measurement-based state vector with the PMU measurements [8–13]. Noninvasive methods however require complete observability by the SCADA telemetering system. On the other hand, the direct techniques do not necessitate SCADA system observability, but rather treat both SCADA and PMU measurements in a unified optimization framework [14–18]. The large disparity in data refresh rates amongst PMU and SCADA measurements is an issue common to all hybrid state estimators; the proposed solutions include buffering PMU measurements [19] and SCADA state reconstruction techniques [20,21].

Recent research has shown that hybrid state estimation can be carried out using the NE approach in complex variables [22], and that the complex variable approach has advantages (i) in handling complex-valued measurements and (ii) in implementation on modern processors that support single instruction multiple data (SIMD) operations [23]. SIMD instructions allow processing multiple pieces of data using a single instruction, thus speeding up the throughput of implementations

* Corresponding author.

E-mail addresses: izdazfic@ieee.org (I. Džafić), rabih.jabr@aub.edu.lb (R.A. Jabr).

for video encoding/decoding, image processing, and data analysis [24]; SIMD instruction sets also allow fused multiply-accumulate operations, which could naturally be leveraged in complex variable computing applications. The complex NE (CNE) approach in [22] is a generalization of the real variable implementation, derived via Wirtinger calculus [25,26]. This paper contributes a complex equality constrained (CEC) estimator that is implemented using advanced vector extensions (AVX-2) [24]. The CEC estimator extends the CNE approach to include equality constraints, and thus effectively handle zero injection measurements for further improving the estimation accuracy and bad data identification; in addition, the AVX-2 implementation allows for a very fast implementation that is commensurate with the requirements of real-time applications. The proposed CEC approach is contrasted with both the CNE approach [22] and the real equality constrained (REC) hybrid state estimator that is based on [14] but modified to exactly model equality constraints.

The rest of this paper is organized as follows. Section 2 reviews the normal equations approach in complex variables, and Section 3 presents the extension to the complex variable normal equations with equality constraints. An introduction to the program implementation via AVX-2 is given in Section 4. Section 5 discusses bad data identification using the largest normalized residual test [2] extended to operate on complex state variables. Section 6 presents numerical results and comparisons with the CNE [22] and REC (modified from [14]) estimators on networks with up to 9241 nodes. The paper is concluded in Section 7.

2. Complex Normal Equations (CNE)

Consider the power system state estimation problem in complex variables (1), where $h(x, \bar{x})$ is the vector of measurement functions, z is the vector of measured values, x is the vector of complex state variables (phasor voltages), and \bar{x} denotes the conjugate of x [22]:

$$h(x, \bar{x}) \approx z \quad (1)$$

$$h \begin{pmatrix} x \\ \bar{x} \end{pmatrix} = \begin{bmatrix} h_1(x, \bar{x}) \\ \vdots \\ h_m(x, \bar{x}) \end{bmatrix}, \quad z = \begin{bmatrix} z_1 \\ \vdots \\ z_m \end{bmatrix} \quad (2)$$

For example, if z_1 is the complex power injection measurement at node i , then the first equation in (1) is:

$$h_1 \begin{pmatrix} x \\ \bar{x} \end{pmatrix} = u_i \bar{y}_{ii} \bar{u}_i + u_i \sum_{k=1}^n \bar{y}_{ik} \bar{u}_k \approx z_1 \quad (3)$$

where

$$Y_{ii} = y_i^{sh} + \sum_{k \neq i}^n y_{ik}, \quad Y_{ik} = -y_{ik}, \quad k \neq i \quad (4)$$

y_{ik} is the series admittance of branch ik , y_i^{sh} is the shunt admittance at node i , u_i is the phasor voltage at node i , and n is the number of nodes. Using Wirtinger calculus, (1) can be linearized via the complex Taylor series expansion around the current estimate of the state vector $[x^*; \bar{x}^*]$; H is formed by the Jacobian H_x and the conjugate Jacobian $H_{\bar{x}}$ matrices evaluated at $[x^*; \bar{x}^*]$:

$$h \begin{pmatrix} x^* \\ \bar{x}^* \end{pmatrix} + H \begin{bmatrix} \Delta x \\ \Delta \bar{x} \end{bmatrix} \approx z \quad (5)$$

$$H = [H_x, H_{\bar{x}}] = \begin{bmatrix} \frac{\partial h_1}{\partial x_1} & \dots & \frac{\partial h_1}{\partial x_n} & \frac{\partial h_1}{\partial \bar{x}_1} & \dots & \frac{\partial h_1}{\partial \bar{x}_n} \\ \vdots & \ddots & \vdots & \vdots & \ddots & \vdots \\ \frac{\partial h_m}{\partial x_1} & \dots & \frac{\partial h_m}{\partial x_n} & \frac{\partial h_m}{\partial \bar{x}_1} & \dots & \frac{\partial h_m}{\partial \bar{x}_n} \end{bmatrix} \quad (6)$$

The correction to the state vector $[\Delta x^*; \Delta \bar{x}^*]$ is obtained by minimizing the weighted least squares (WLS) objective value:

$$\ell \begin{pmatrix} \Delta x \\ \Delta \bar{x} \end{pmatrix} = \frac{1}{2} \left(\bar{r} - \bar{H} \begin{bmatrix} \Delta \bar{x} \\ \Delta x \end{bmatrix} \right)^T W \left(r - H \begin{bmatrix} \Delta x \\ \Delta \bar{x} \end{bmatrix} \right) \quad (7)$$

where W is a diagonal matrix of measurement weights and $r = z - h(x^*, \bar{x}^*)$. Eq. (7) can be expanded into (8), with the vector β and matrix G given by (9) and (10), respectively:

$$\ell = \frac{1}{2} \left(\bar{r}^T W r - \bar{\beta}^T \begin{bmatrix} \Delta x \\ \Delta \bar{x} \end{bmatrix} - [\Delta \bar{x}^T \quad \Delta x^T] \beta \right) + \frac{1}{2} \left([\Delta \bar{x}^T \quad \Delta x^T] G \begin{bmatrix} \Delta x \\ \Delta \bar{x} \end{bmatrix} \right) \quad (8)$$

$$\beta = \bar{H}^T W r = \begin{bmatrix} \beta_{\bar{x}} \\ \beta_x \end{bmatrix} \quad (9)$$

$$G = \bar{H}^T W H = \begin{bmatrix} G_{\bar{x}\bar{x}} & G_{\bar{x}x} \\ G_{x\bar{x}} & G_{xx} \end{bmatrix} \quad (10)$$

Ref. [22] shows that for hybrid power system state estimation, the elements of G and β satisfy the following properties: $\beta_x = \bar{\beta}_{\bar{x}}$, $G_{x\bar{x}} = \bar{G}_{\bar{x}x} = G_{\bar{x}x}^T$, and $G_{xx} = G_{\bar{x}\bar{x}}^T = \bar{G}_{\bar{x}\bar{x}}^T$. Then the minimizer of (8) is given by the solution of the normal equations:

$$G \begin{bmatrix} \Delta x \\ \Delta \bar{x} \end{bmatrix} = \beta \quad (11)$$

3. Complex Equality Constrained (CEC) normal equations

The zero injection measurements give rise to a large disparity of weights in the normal equations approach, and may lead to severe ill-conditioning [1]. This problem can be alleviated by a constrained WLS method, which treats zero injection measurements as equality constraints. The zero injection at node i is modeled by the complex power injection ($s_i(x, \bar{x}) = 0$) and its conjugate ($\bar{s}_i(x, \bar{x}) = 0$), leading to the following relationship between their Wirtinger derivatives [26]:

$$\frac{\partial \bar{s}_i}{\partial x_j} = \overline{\left(\frac{\partial s_i}{\partial \bar{x}_j} \right)}, \quad \frac{\partial \bar{s}_i}{\partial \bar{x}_j} = \overline{\left(\frac{\partial s_i}{\partial x_j} \right)} \quad (12)$$

Therefore, the constrained linear WLS problem can be written as:

$$\min \ell(\Delta x, \Delta \bar{x}) \quad (13)$$

subject to a linear approximation of the zero complex power injection equations and their conjugates:

$$J \begin{bmatrix} \Delta x \\ \Delta \bar{x} \end{bmatrix} = \begin{bmatrix} J_x & J_{\bar{x}} \\ \bar{J}_{\bar{x}} & \bar{J}_x \end{bmatrix} \begin{bmatrix} \Delta x \\ \Delta \bar{x} \end{bmatrix} = \begin{bmatrix} -s \\ -\bar{s} \end{bmatrix} \quad (14)$$

where the elements in the complex vectors s and \bar{s} contain the equations for the zero complex power injections and their conjugates; the corresponding equations are given in the Appendix A, which also includes the slack angle condition. The classical theory of Lagrange multipliers for solving constrained minimization problems stipulates that the objective function and constraints are real-valued functions of real unknown variables; however by applying Wirtinger calculus, [26] shows

that a stationary point of the Lagrangian function (15) is a solution to (13) and (14), where \Re denotes the real part of a complex quantity:

$$\mathcal{L} = \ell(\Delta x, \Delta \bar{x}) + \Re \left\{ [\bar{\lambda}^T, \lambda^T] \left(\begin{bmatrix} J_x & J_{\bar{x}} \\ \bar{J}_x & J_x \end{bmatrix} \begin{bmatrix} \Delta x \\ \Delta \bar{x} \end{bmatrix} + \begin{bmatrix} s \\ \bar{s} \end{bmatrix} \right) \right\} \quad (15)$$

Theorem 1. The solution to the complex constrained linear WLS problem (13) and (14) that arises in hybrid power system state estimation is given by the normal equations with equality constraints:

$$\begin{bmatrix} G_{\bar{x}x} & G_{\bar{x}\bar{x}} & \bar{J}_x^T & J_x^T \\ \bar{G}_{\bar{x}x} & \bar{G}_{\bar{x}\bar{x}} & \bar{J}_x^T & J_x^T \\ J_x & J_{\bar{x}} & 0 & 0 \\ \bar{J}_x & \bar{J}_{\bar{x}} & 0 & 0 \end{bmatrix} \begin{bmatrix} \Delta x \\ \Delta \bar{x} \\ \lambda \\ \bar{\lambda} \end{bmatrix} = \begin{bmatrix} \beta_{\bar{x}} \\ \bar{\beta}_{\bar{x}} \\ -s \\ -\bar{s} \end{bmatrix} \quad (16)$$

Proof. Eq. (17) shows that the function in parenthesis in (15) is real:

$$\begin{aligned} & [\bar{\lambda}^T, \lambda^T] \left(\begin{bmatrix} J_x & J_{\bar{x}} \\ \bar{J}_x & J_x \end{bmatrix} \begin{bmatrix} \Delta x \\ \Delta \bar{x} \end{bmatrix} + \begin{bmatrix} s \\ \bar{s} \end{bmatrix} \right) \\ &= \underbrace{\bar{\lambda}^T J_x \Delta x + \lambda^T J_{\bar{x}} \Delta \bar{x}}_{2\Re\{\bar{\lambda}^T J_x \Delta x\}} + \underbrace{\bar{\lambda}^T J_{\bar{x}} \Delta \bar{x} + \lambda^T J_x \Delta x}_{2\Re\{\bar{\lambda}^T J_{\bar{x}} \Delta \bar{x}\}} + \underbrace{\bar{\lambda}^T s + \lambda^T \bar{s}}_{2\Re\{\bar{\lambda}^T s\}} \end{aligned} \quad (17)$$

Using (17), the Lagrangian function (15) reduces to:

$$\mathcal{L} = \ell(\Delta x, \Delta \bar{x}) + [\bar{\lambda}^T, \lambda^T] \left(\begin{bmatrix} J_x & J_{\bar{x}} \\ \bar{J}_x & J_x \end{bmatrix} \begin{bmatrix} \Delta x \\ \Delta \bar{x} \end{bmatrix} + \begin{bmatrix} s \\ \bar{s} \end{bmatrix} \right) \quad (18)$$

Therefore:

$$\nabla_{\Delta \bar{x}} \mathcal{L} = \nabla_{\Delta \bar{x}} \ell + [\bar{\lambda}^T J_{\bar{x}} + \lambda^T J_x]^T = -\bar{\beta}_{\bar{x}} + G_{\bar{x}x} \Delta x + G_{\bar{x}\bar{x}} \Delta \bar{x} + \bar{J}_x^T \lambda + J_x^T \bar{\lambda} \quad (19)$$

$$\nabla_{\Delta x} \mathcal{L} = \nabla_{\Delta x} \ell + [\bar{\lambda}^T J_x + \lambda^T \bar{J}_x]^T = -\beta_x + \bar{G}_{\bar{x}x} \Delta x + \bar{G}_{\bar{x}x} \Delta \bar{x} + \bar{J}_x^T \lambda + J_x^T \bar{\lambda} \quad (20)$$

Equating (19) and (20) to zero, together with the feasibility constraints (14), results in a set of equations that is necessary and sufficient to compute a stationary point of \mathcal{L} (a minimizer of (13) and (14) due to the convexity of the problem); these conditions are given in (16). It stays to demonstrate that the solution to (16) gives two pairs of complex conjugate vectors, $[\Delta x; \Delta \bar{x}]$ and $[\lambda; \bar{\lambda}]$. To show this, write (16) as:

$$\begin{bmatrix} G_{\bar{x}x} & G_{\bar{x}\bar{x}} & \bar{J}_x^T & J_x^T \\ \bar{G}_{\bar{x}x} & \bar{G}_{\bar{x}\bar{x}} & \bar{J}_x^T & J_x^T \\ J_x & J_{\bar{x}} & 0 & 0 \\ \bar{J}_x & \bar{J}_{\bar{x}} & 0 & 0 \end{bmatrix} \begin{bmatrix} \Delta x \\ \Delta \bar{x} \\ \lambda \\ \mu \end{bmatrix} = \begin{bmatrix} \beta_{\bar{x}} \\ \bar{\beta}_{\bar{x}} \\ -s \\ -\bar{s} \end{bmatrix} \quad (21)$$

Taking the complex conjugate of (21) gives:

$$\begin{bmatrix} \bar{G}_{\bar{x}x} & \bar{G}_{\bar{x}\bar{x}} & \bar{J}_x^T & \bar{J}_x^T \\ G_{\bar{x}x} & G_{\bar{x}\bar{x}} & \bar{J}_x^T & \bar{J}_x^T \\ \bar{J}_x & \bar{J}_{\bar{x}} & 0 & 0 \\ J_x & J_{\bar{x}} & 0 & 0 \end{bmatrix} \begin{bmatrix} \Delta \bar{x} \\ \Delta y \\ \bar{\lambda} \\ \bar{\mu} \end{bmatrix} = \begin{bmatrix} \bar{\beta}_{\bar{x}} \\ \beta_{\bar{x}} \\ -\bar{s} \\ -s \end{bmatrix} \quad (22)$$

Swapping as a whole the first row with the second (in (22)), the third row with the fourth, the first column with the second, and the third column with the fourth gives:

$$\begin{bmatrix} G_{\bar{x}x} & G_{\bar{x}\bar{x}} & \bar{J}_x^T & \bar{J}_x^T \\ \bar{G}_{\bar{x}x} & \bar{G}_{\bar{x}\bar{x}} & \bar{J}_x^T & \bar{J}_x^T \\ J_x & J_{\bar{x}} & 0 & 0 \\ \bar{J}_x & \bar{J}_{\bar{x}} & 0 & 0 \end{bmatrix} \begin{bmatrix} \Delta \bar{y} \\ \Delta \bar{x} \\ \bar{\mu} \\ \bar{\lambda} \end{bmatrix} = \begin{bmatrix} \beta_{\bar{x}} \\ \bar{\beta}_{\bar{x}} \\ -s \\ -\bar{s} \end{bmatrix} \quad (23)$$

Now comparing (23) with (21) shows that $\Delta y = \Delta \bar{x}$ and $\mu = \bar{\lambda}$, i.e. the solution to (16) gives a pair of complex conjugate solutions and is

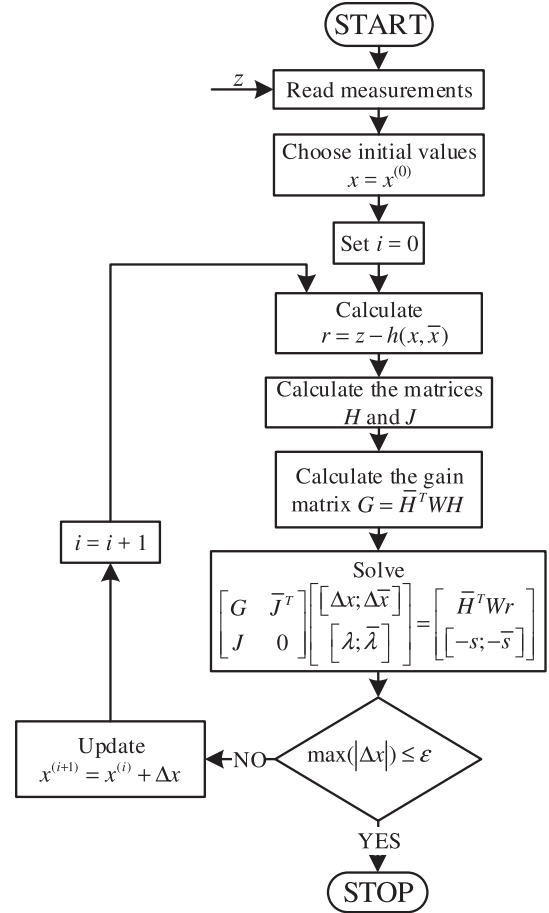


Fig. 1. Hybrid SE via Complex Equality Constrained (CEC) normal equations.

therefore admissible. \square

Theorem 1 reveals that the complex normal equations with equality constraints (CEC) has a form analogous to the real variable EC estimator. The flowchart for the CEC method is given in Fig. 1; it is simple enough to be easily adopted for practical implementation. The method starts by reading the SCADA/PMU measurements and choosing an initial estimate $x^{(0)}$ of the state vector, which could be a flat start. The iteration counter i is initialized to zero, and the corresponding vector of measurement residuals r is calculated together with the matrices H , J , and G as given by (10); this is followed by solving (16). If the maximum magnitude of any element in the vector Δx is less than a pre-specified tolerance ϵ , the algorithm terminates with the state vector estimate; otherwise, the state vector is updated using $x^{(i+1)} = x^{(i)} + \Delta x$, the iteration counter is incremented by 1, and the algorithm proceeds by solving (16) with the updated values for the matrices and vectors. The Appendix A of this paper shows the elements of the J matrix, whereas the elements of H that are required in forming the G matrix are available in [22].

4. Advanced Vector Extensions: AVX-2

Modern processors support single instruction multiple data (SIMD) processor extensions, which include Advanced Vector Extensions - AVX2 [24]. AVX2 uses 256-bit registers and therefore allows the manipulation of two double precision complex values (two real and two imaginary parts) per register of CPU; this results in fast arithmetic

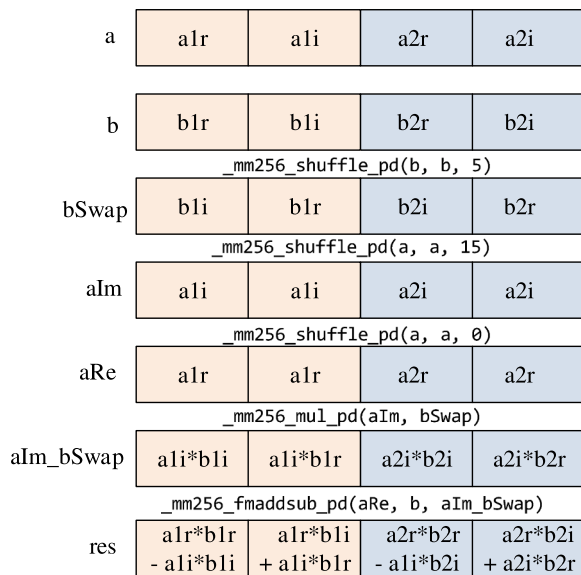


Fig. 2. Vectorized complex multiplication using AVX-2.

operations with complex numbers, and makes AVX-2 ideal for implementing real-time estimation and control functions in complex variables.

Consider for illustration the product of two complex numbers:

$$(a1r + i * a1i) * (b1r + i * b1i) = (a1r * b1r - a1i * b1i) + i * (a1r * b1i + a1i * b1r) \quad (24)$$

```
// AVX2 with fused-multiply-add intrinsics
// requires only two multiplications to multiply
// two double precision complex numbers
```

```
__m256d mult(__m256d const& a, __m256d const& b)
{
    // Swap b.re and b.im
    __m256d bSwap = _mm256_shuffle_pd(b, b, 5);
    // Imag part of a in both
    __m256d aIm = _mm256_shuffle_pd(a, a, 15);
    // Real part of a in both
    __m256d aRe = _mm256_shuffle_pd(a, a, 0);
    // First multiplication (a.im*b.im, a.im*b.re)
    __m256d aIm_bSwap = _mm256_mul_pd(aIm, bSwap);
    // Second multiplication with fused add/sub
    // aRe*b + complex(-aIm_bSwap.re, aIm_bSwap.im)
    return _mm256_fmaddsub_pd(aRe, b, aIm_bSwap);
}
```

From an implementation perspective, the non-vectorized multiplication in (24) would require 4 multiplication steps, 1 addition step, and 1 subtraction step; when performing two complex number multiplications $(a1r + i * a1i) * (b1r + i * b1i)$ and $(a2r + i * a2i) * (b2r + i * b2i)$, the non-vectorized code would therefore require 8 multiplication steps, 2 addition steps, and 2 subtraction steps. In contrast, the AVX-2 code in Algorithm 1 performs the same multiplication but using 2 multiplication steps (each step involves 4 simultaneous multiplications), 1 addition/subtraction step, and 3 register shuffles. Fig. 2 illustrates the corresponding steps in the 256-bit CPU registers. In Fig. 2, a is a 256-bit register holding two complex numbers $((a1r + i * a1i)$ and $(a2r + i * a2i)$), where each of the real and imaginary components are stored in a 64-bit register block; similarly, the 256-bit register b contains two complex numbers $((b1r + i * b1i)$ and $(b2r + i * b2i)$). To achieve the multiplication, four intermediate results are stored in four 256-bit registers: register bSwap contains the swapped elements of b, registers aIm and aRe contain only duplicates of the imaginary and real parts of a, and the register aIm_bSwap holds the block register multiplication of aIm and bSwap. The result of the multiplication is in the register res; it is formed using the fused multiply add/subtract function which takes the multiplication of aRe and b, and adds/subtracts the block registers (2 and 4)/(1 and 3) of aIm_bSwap. The fused multiply add/subtract function is particularly targeted to complex number operations; it allows faster multiplication of two complex (double precision) numbers by two complex numbers.

AVX-2 includes several advances related to the new fused-multiply-add (FMA) instructions; these have been leveraged in the implementation of the CEC estimator in Fig. 1.

Algorithm 1. Computation of two complex values using double precision AVX-2 with Fuse-Multiply-Add intrinsics

Table 1
Network measurement sets.

Net.	Topology		Measurements			
	#nodes	#branches	#SCADA	#V-PMU	#I-PMU	#ZeroInj
118_A	118	186	372	4	3	10
118_B	118	186	372	3	35	10
118_C	118	186	372	3	186	10
118_D	118	186	0	118	186	10
1888_A	1888	2531	5060	2	0	680
1888_B	1888	2531	5060	4	154	680
1888_C	1888	2531	5060	87	1261	680
1888_D	1888	2531	0	1888	2531	680
9241_A	9241	16,049	32,098	17	89	2901
9241_B	9241	16,049	32,098	38	2007	2901
9241_C	9241	16,049	32,098	66	8025	2901
9241_D	9241	16,049	0	9241	16,049	2901

5. Bad data identification

In the case when χ^2 test detects the existence of bad data in the measurement set, further processing is required to identify the erroneous measurements. The bad data identification is accomplished by using the Largest Normalized Residual (LNR) test [2], adjusted to the complex state variable set:

1. Solve the state estimation problem and calculate the measurement residual vector:

$$r_i = z_i - h_i(\hat{x}), \quad i = 1, \dots, m \quad (25)$$

2. Calculate the diagonal entries of the residual covariance matrix Ω . The process is described in the following steps:

(a) Factorize the gain matrix G using Cholesky factorization: $G = LL^T$

(b) Calculate the column entries of the temporary matrix T by using the i -th row of the measurement Jacobian matrix H , and solving:

$$LL^T T_i = \bar{h}_i^T \quad i = 1, \dots, m \quad (26)$$

Note that this step differs from [2], in the sense that it employs the complex conjugate transpose instead of the simple transpose.

(c) Compute the diagonal entries of the residual covariance matrix for each measurement:

$$\Omega_{ii} = \frac{1}{W_{ii}} - h_i T_i \quad (27)$$

where W_{ii} is the weight of measurement i and the values of Ω_{ii} are always real numbers.

3. Compute the normalized residuals

$$r_i^n = \frac{|r_i|}{\sqrt{\Omega_{ii}}} \quad (28)$$

4. Find k such that r_k^n is the largest among all r_i^n .
5. If $r_k^n \geq c$ where c is the identification threshold, then the k -th measurement is considered as bad data; otherwise, stop.
6. Eliminate the k -th measurement from the set of measurements and go to step 1.

6. Numerical results

The CEC state estimator was programmed in C++, and the computations were performed using solvers developed via the AVX-2 processor extension [24]. Comparative analysis was carried out with the

CNE implementation in [22] (see Section 2), and with an implementation of the real variable equality constrained (REC) hybrid state estimator for handling both SCADA and PMU measurements; the REC implementation is based on [14] but modified to handle virtual measurements such as zero injections via standard equality constrained WLS state estimation [2]. The CEC estimator employs LDL^T factorization of the indefinite Hermitian matrix in (16) while preserving conjugate symmetry; this is carried out via a Bunch-Kaufman block-pivot approach that resorts to 1×1 and 2×2 pivots [2]. However, for CNE that factorizes the gain matrix in (10), Cholesky decomposition is employed.

The numerical tests were executed on a PC with an Intel i5-7600 K processor and 16 GB of RAM. The termination tolerance ϵ in Fig. 1 was set to 10^{-6} per-unit. The testing was carried out on the IEEE 118 test network (118), the French very high-voltage 1888 node network (1888), and part of the European high voltage transmission network with 9241 nodes [27]. The network information is summarized in Table 1, and it includes for each network four instances of measurement placement (denoted by A, B, C, and D) with increasing number of PMU devices; columns 4 to 7 show the number of SCADA measurements, voltage PMU measurements, current PMU measurements, and zero injection measurements (when employed); the complete data sets are available for download from [28]. When using PMUs, the nodal voltage angles are all measured with respect to a common reference dictated by the GPS. The choice of a reference angle or bus is not arbitrary. There are two main possibilities [18,29]:

- (a) Choose a bus where a PMU is present as the reference bus. This choice assumes that the PMU at the reference bus works perfectly; it effectively subtracts the angle of the reference bus nodal voltage (relative to the reference dictated by the GPS) from all nodal voltage angles, thus setting the reference bus angle to zero. The choice of having a reference bus with zero angle is common in the traditional SE formulations that employ only SCADA measurements.
- (b) Choose the common GPS reference for all nodal voltage angles; this will allow using the absolute phase angles given by the PMUs. Note that in the presence of a single PMU, this choice can be reduced to the conventional case with a reference bus (case (a) above) and any error in the PMU measurement angle will not affect the estimation results.

Both possibilities above could be integrated into the proposed CEC estimator, and phasor current angles can be defined relative to any of these references. The results in the paper are reported for option (a), as this is the option used in the previously published REC [14] and CNE [22] estimators covered in the numerical comparison; references [15,16] also report numerical simulations using option (a). Note however that the two possibilities (a) and (b) lead to different PMU phase-angle measurement uncertainties (or equivalent ones), and the two choices could lead to different performance.

The percentage standard deviation of the measurements are given in Table 2 together with the weights. The error is simulated as Gaussian noise with zero mean and a per-unit standard deviation computed as a percentage of the meter full-scale reading. Note that the weights are chosen to be consistent with [22], and are normalized so that the minimum value is 1 to improve numerical conditioning; the weights of

Table 2
Measurement standard deviations and weights.

	SCADA Measurements			PMU Measurements			ZI
	Voltage	inj. power	Power flows	Voltage	Current	ph. angle	Meas.
Std.Dev.	2%	2%	2%	0.5%	0.5%	0.1°	0
Weight	1	1	1	5	5	5	25

the zero injection measurements are needed for the CNE estimator, but not for the CEC and REC implementations that have the zero injection measurements handled as equality constraints.

Table 3 shows the sparse matrix information and computational performance of CEC relative to CNE for the case without zero injection measurements, and Table 4 for the case with zero injection measurements. The sparse matrix information for the CNE/CEC estimator includes the dimension of the gain/Jacobian matrix and its number of upper diagonal matrix non-zeros (NZ). Although both the CEC and CNE methods employ the zero angle reference at a bus with a PMU, the enforcement of the reference bus condition is slightly different in the implementations. For the CEC, the zero angle condition is modeled by having an equality constraint that sets the imaginary part of the voltage at the reference bus to zero. However, for CNE, the same equality constraint is treated as a virtual measurement with high weight, similar to the practice of handling zero injection measurements in CNE. The difference in the implementations explains why for the case without zero injection measurements (Table 3), the size and number of non-zeros of the CEC estimator are higher than the corresponding CNE quantities by only 1.

The CNE estimator computational results in Table 3 correspond to the same network and measurement sets in [22], but averaged over 200 simulations of Gaussian noise; the CEC results show a speed-up factor (SUF = time CNE/time CEC) that approaches 1.57. For the estimation results with zero injection measurements as shown in Table 4, the SUF factor also approaches a maximum value of around 1.49 with the execution times averaged over 200 trials. Table 5 reports the minimum and maximum execution times corresponding to the average values in Tables 3 and 4; the range of variation is relatively narrow over the two hundred trials with different measurement noise. Note that the CEC estimator computing time on the largest instance is less than 300 ms, making it suitable for real time applications. The CNE implementation [22] uses solvers developed in house via the SIMD instruction set, without AVX-2. The difference in implementations between CEC and CNE explains why CEC is faster than CNE, even without zero-injection measurements. The time values in Tables 3–5 were obtained using the high-resolution clock in Algorithm 2, which forms part of the C++11 standard.

Algorithm 2. Timer

```
#include <chrono>
//this is part of C++11 standard
//https://en.cppreference.com/w/cpp/chrono/high_resolution_clock/now
...
//get start time
auto start = std::chrono::high_resolution_clock::now();
... //here comes SE code
//get end time
auto end = std::chrono::high_resolution_clock::now();
//calculate time difference
std::chrono::duration<double> diff = end-start;
```

In addition to the AVX-2 CEC implementation being faster than the recent CNE implementation in [22], the CEC estimator is also more accurate than the CNE due to the exact modeling of zero injection measurements. The accuracy is quantified using performance indices for the measurement error (29) and the voltage error (30) [16]:

$$\xi_z = \frac{\sum_{i=1}^m |z_i^{\text{estimated}} - z_i^{\text{true}}|^2}{\sum_{i=1}^m |z_i^{\text{measured}} - z_i^{\text{true}}|^2} \quad (29)$$

$$\sigma_x^2 = \sum_{i=1}^n |x_i^{\text{estimated}} - x_i^{\text{true}}|^2 \quad (30)$$

For estimation with zero injection measurements, Tables 6 and 7 respectively show the performance indices for the measurement error and voltage error. For each network in these tables, the performance indices are computed after the state vector is estimated via the CEC, the CNE [22], and the REC (modified from [14]) methods. Two performance improvement factor (PIF) ratios are used to quantify how the measurement (29) and voltage (30) performance indices of the CNE and REC estimators compare against CEC; these ratios are:

$$\text{PIF} - \text{CNE} = \frac{\text{performance index of CNE}}{\text{performance index of CEC}} \quad (31)$$

$$\text{PIF} - \text{REC} = \frac{\text{performance index of REC}}{\text{performance index of CEC}} \quad (32)$$

The results in Tables 6 and 7 show that both the PIF – CNE and PIF – REC indices are consistently greater than 1, and that the performance improvement exceeds 3 when evaluated for the CNE measurement accuracy. The square root of the measurement error ($\sqrt{\xi_z}$) and voltage error (σ_x) accuracy indices are depicted graphically in Figs. 3 and 4, together with the corresponding performance improvement factors. In the comparison between the CEC and REC, the performance improvement factors remain close to 1; this is because both methods use equivalent state vectors and equality constraints in their implementations.

6.1. Performance under increased loading

The CEC estimator also exhibits superior computational perfor-

Table 3
Sparse matrix information and computational performance of CNE/CEC without zero injection measurements (average over 200 runs).

Net.	Matrix Size		Matrix #NZ		#Iteration		Time [ms]		SUF
	CNE	CEC	CNE	CEC	CNE	CEC	CNE	CEC	
118_A	236	237	1052	1054	4.00	4.00	1.1	0.9	1.22
118_B	236	237	1052	1054	4.00	4.00	1.3	1.13	1.15
118_C	236	237	1052	1054	4.00	4.00	1.4	1.17	1.20
118_D	236	237	595	596	1.00	1.00	0.4	0.4	1.00
1888_A	3776	3777	14,121	14,123	5.11	5.11	26.4	23.4	1.13
1888_B	3776	3777	14,121	14,123	5.00	5.00	28.4	24.5	1.16
1888_C	3776	3777	14,121	14,123	4.00	4.00	22.3	18.1	1.23
1888_D	3776	3777	8393	8394	1.00	1.00	5.3	5.0	1.05
9241_A	18,482	18,483	82,127	82,128	5.00	5.00	312.7	189.3	1.65
9241_B	18,482	18,483	82,127	82,128	5.00	5.00	308.6	188.7	1.64
9241_C	18,482	18,483	82,127	82,128	5.00	5.00	311.4	198.8	1.57
9241_D	18,482	18,483	46,897	46,898	1.00	1.00	50.3	45.2	1.11

mance under stressed conditions leading to voltage instability [30], as evidenced by the results in Table 8; in this table, the load of the 1888_A test instance is uniformly increased and both the CEC and REC methods are used to estimate the state with a tighter tolerance of 10^{-7} per-unit. At the highest load multiplication factor of 1.077, the CEC estimator required 7 iterations to converge while the REC required 10; the corresponding convergence pattern is shown in Table 9. The CEC estimator therefore improves precision with reduced computational requirements; this makes it suitable in applications for improving the quality of state estimation [31] and enhancing the processing of bad data [32]. The result of state estimation is employed when running energy management system (EMS) functions, including optimal power flow applications and network what-if scenario analysis. The EMS functions would give solutions that more clearly reflect the actual operation of the system when they employ more accurate estimates of the current operating point, including the nodal loads. Note that the results in Table 8 are intended to show the numerical performance of the CEC and REC methods under increased loading; they are reported for one run with exact measurements.

6.2. Bad data identification

The Largest Normalized Residual (LNR) test in Section 5 was used to demonstrate the effect that the exact handling of zero injection measurements has on bad data identification. The same networks with measurement scenarios A, B, and C were simulated with bad data, and each under 200 instances of Gaussian noise. The bad data in each network constituted of a real power branch measurement that is

Table 4
Sparse matrix information and computational performance of CNE/CEC with zero injection measurements (average over 200 runs).

Net.	Matrix Size		Matrix #NZ		#Iteration		Time [ms]		SUF
	CNE	CEC	CNE	CEC	CNE	CEC	CNE	CEC	
118_A	236	257	1146	1162	4.00	4.00	1.46	1.42	1.03
118_B	236	257	1146	1162	4.00	4.00	1.50	1.46	1.03
118_C	236	257	1146	1162	3.96	3.95	1.65	1.54	1.07
118_D	236	257	759	704	3.00	3.00	0.88	0.84	1.05
1888_A	3776	5137	20,960	21,106	5.00	5.00	49.17	45.53	1.08
1888_B	3776	5137	20,960	21,106	5.00	5.00	51.48	45.96	1.12
1888_C	3776	5137	20,960	21,081	5.00	5.00	55.40	47.76	1.16
1888_D	3776	5137	18,971	15,378	4.00	4.00	33.93	31.71	1.07
9241_A	18,482	24,285	100,903	108,594	5.00	5.00	381.85	267.30	1.43
9241_B	18,482	24,285	100,903	108,654	5.00	5.00	405.85	272.54	1.49
9241_C	18,482	24,285	100,903	108,716	5.00	5.00	412.61	283.67	1.45
9241_D	18,482	24,285	80,116	73,646	4.00	4.00	247.12	180.74	1.37

Table 5
Min/Max solution times (min/max over 200 runs).

Net.	Without ZI				With ZI			
	CNE [ms]		CEC [ms]		CNE [ms]		CEC [ms]	
	min	max	min	max	min	max	min	max
118_A	1.0	1.2	0.8	1.0	1.3	1.6	1.3	1.5
118_B	1.2	1.4	1.0	1.2	1.4	1.7	1.3	1.6
118_C	1.2	1.5	1.1	1.3	1.5	1.8	1.4	1.7
118_D	0.4	0.5	0.4	0.5	0.8	0.9	0.8	0.9
1888_A	24.3	33.2	19.5	28.9	47.5	52.3	42.6	48.1
1888_B	25.7	30.7	22.1	27.7	48.3	53.9	42.6	49.0
1888_C	19.8	24.6	16.3	19.7	52.6	58.7	43.8	50.2
1888_D	4.9	5.6	4.8	5.2	31.1	36.2	30.2	33.8
9241_A	303.7	320.7	185.5	194.8	368.6	395.7	263.1	272.7
9241_B	299.8	318.7	183.6	192.9	395.8	414.2	263.8	278.4
9241_C	302.3	321.0	194.3	204.6	403.2	419.3	277.5	288.6
9241_D	48.3	52.4	43.7	48.1	244.8	253.0	177.4	184.3

multiplied by a factor of -1.5 or -2 , and then placed on the opposite side of the branch. Table 10 shows the minimum and maximum values of the LNR, as observed over 200 instances of simulated noise and for the two multiplying factors that represent bad data. In the LNR test, bad data is suspected in a measurement z_k whenever the LNR corresponds to z_k and is greater than a preselected identification threshold. Therefore, it is always better to have a greater value of the LNR for

Table 6
Measurement performance accuracy indices with zero injection measurements (average over 200 runs).

Net.	CEC	CNE	PIF-CNE	REC	PIF-REC
118_C	0.043730	0.043903	1.004	0.043841	1.003
118_D	0.006822	0.007237	1.061	0.006868	1.007
1888_C	0.180213	0.184422	1.034	0.181573	1.008
1888_D	0.002982	0.006496	2.178	0.003005	1.008
9241_C	0.133647	0.154353	1.155	0.135721	1.016
9241_D	0.001161	0.003526	3.037	0.001192	1.027

Table 7
Voltage performance accuracy indices with zero injection measurements (average over 200 runs).

Net.	CEC	CNE	PIF-CNE	REC	PIF-REC
118_C	0.000936	0.000951	1.016	0.000939	1.003
118_D	0.000074	0.000079	1.068	0.000076	1.027
1888_C	0.032794	0.033116	1.010	0.032921	1.004
1888_D	0.004831	0.005756	1.191	0.004879	1.010
9241_C	0.092998	0.099949	1.075	0.093606	1.007
9241_D	0.020224	0.022186	1.097	0.020875	1.032

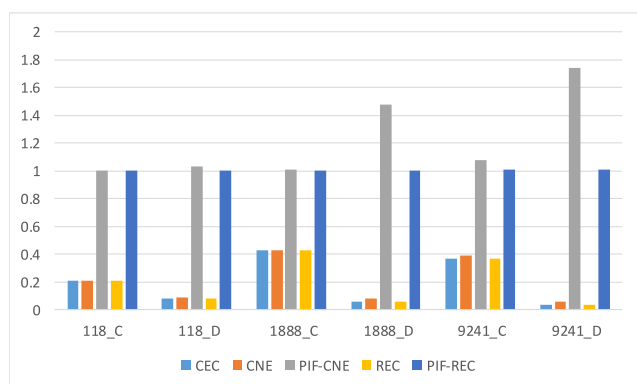


Fig. 3. Measurement performance accuracy indices ($\sqrt{\xi_z}$).

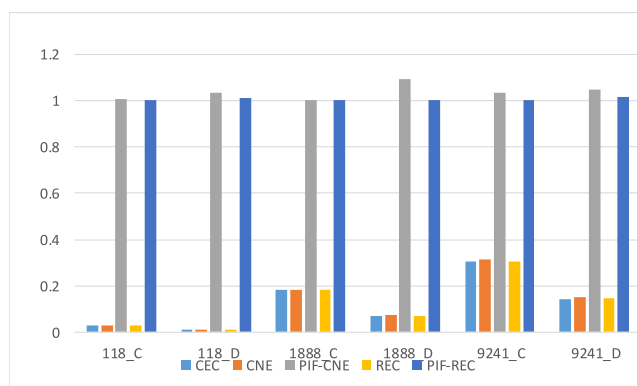


Fig. 4. Voltage performance accuracy indices (σ_v).

identifying bad data in a measurement. Table 10 demonstrates that the minimum/maximum values of the observed LNR are consistently greater when using the CEC estimator as compared to CNE. In addition, columns 5 and 8 of the table show the percentage increase (Δ) in the LNR values when using CEC instead of CNE; these results illustrate that the improvement in the LNR values that is attributed to the CEC estimator can reach around 15%. The CEC estimator is therefore more advantageous than CNE when used for bad data identification.

Table 8
Numerical stability test of the CEC and REC estimators on the 1888_A network instance ($\epsilon = 10^{-7}$).

Mult.	Min. Voltage		#Iter.	
	Node No.	Value	CEC	REC
1.000	1194	0.83151	5	5
1.050	1194	0.81383	6	6
1.054	1194	0.81177	7	7
1.070	1194	0.80110	7	7
1.072	1194	0.79914	7	8
1.077	358	0.76614	7	10

Table 9
Convergence pattern of the CEC and REC estimators on the 1888_A network instance with a load multiplier of 1.077 ($\epsilon = 10^{-7}$).

Iteration	Precision	
	CEC	REC
1	1.48116e+00	1.48116e+00
2	1.19273e+00	2.80432e+00
3	5.41629e-01	7.01989e-01
4	1.71176e-01	9.49265e-01
5	1.01962e-02	1.89207e+00
6	1.45915e-04	4.73186e-01
7	1.03513e-08	3.99074e-02
8		4.67715e-03
9		1.89782e-06
10		2.83609e-12

Table 10
Largest normalized residual test using the CEC and CNE estimators.

Net.	Mult.	Min. LNR			Max. LNR		
		CEC	CNE	Δ [%]	CEC	CNE	Δ [%]
118_A	1.5	1.51226	1.48103	2.11	1.60877	1.51469	6.21
	2.0	3.18161	3.06453	3.82	3.37389	3.24922	3.84
118_B	1.5	1.53416	1.49072	2.91	1.69615	1.53894	10.22
	2.0	3.22201	2.92061	10.32	3.41269	3.30736	3.18
118_C	1.5	2.55625	2.49305	2.54	1.71888	1.64710	4.36
	2.0	4.16509	4.02885	3.38	4.32052	4.17916	3.38
1888_A	1.5	6.28437	5.47731	14.73	6.32736	5.51477	14.73
	2.0	12.63272	11.01697	14.67	12.94873	11.29313	14.66
1888_B	1.5	6.63121	5.74239	15.48	6.93076	5.84239	18.63
	2.0	13.09229	11.33895	15.46	13.81802	12.25107	12.79
1888_C	1.5	7.32742	6.40671	14.37	7.97106	6.95035	14.69
	2.0	14.36466	12.92915	11.10	14.51966	12.98284	11.84
9241_A	1.5	3.31646	3.11277	6.54	3.87483	3.67045	5.57
	2.0	6.77997	6.56947	3.20	7.39469	7.08293	4.40
9241_B	1.5	3.43970	3.23233	6.42	3.86378	3.65392	5.74
	2.0	6.99754	6.76844	3.38	7.41659	7.19428	3.09
9241_C	1.5	5.46237	5.24481	4.15	5.87536	5.75674	2.06
	2.0	11.50221	11.06539	3.95	11.92984	11.69180	2.04

Table 11 shows similar results for bad data identification but with two bad data measurements. Four cases are considered for the 1888_C system, each simulated 200 times:

- P + Q: one bad data in a real power measurement and one in a reactive power measurement. In the 200 runs, the locations of the bad data measurements are randomly changed, whereas the errors are set at 50% relative to the measured value with noise.
- phiI + P: one bad data in a phasor current measurement and one in a real power measurement. The error in the real power is simulated as above, whereas the error for the phasor current is sampled from the hollow disk in Fig. 5 whose inner and outer radii are respectively at

Table 11
Multiple bad data identification (200 runs, 1888_C).

Bad Data	#	Min. LNR			Max. LNR			Avg. LNR		
		CEC	CNE	Δ [%]	CEC	CNE	Δ [%]	CEC	CNE	Δ [%]
P + Q	1	2.070	2.040	1.505	9.054	8.082	27.844	7.217	5.537	30.338
	2	2.055	2.025	1.490	8.662	7.498	15.523	4.699	3.723	26.217
pH + P	1	7.559	6.832	10.645	31.202	14.947	108.745	21.275	12.392	71.688
	2	5.760	5.429	6.095	9.593	7.561	26.877	7.939	6.899	15.075
pH + Q	1	6.531	6.368	2.558	32.020	15.143	111.449	19.295	10.764	79.254
	2	2.978	1.948	52.869	9.289	6.505	42.801	4.006	2.613	53.342
pH + pH	1	4.991	4.179	19.446	15.728	7.703	104.167	10.196	6.181	64.964
	2	3.776	2.776	36.044	15.114	7.553	100.087	6.203	4.504	37.717

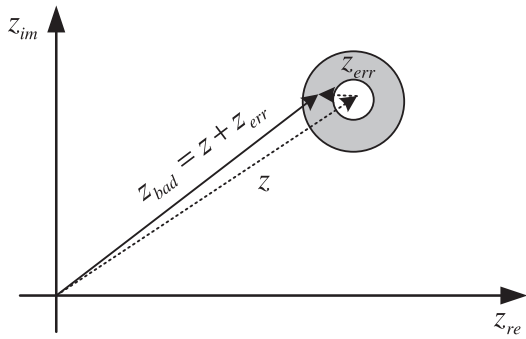


Fig. 5. Simulation of bad PMU measurements.

40% and 50% of the measured magnitude with noise. The phasor currents are again chosen randomly from the set of measurements.

- pH + Q: this case is similar to pH + P, but it employs reactive power instead of real power measurements for simulating bad data.
- pH + pH: this case is again identical to the above, but it simulates error in two phasor current measurements.

Note that cases involving bad data in phasor voltage measurements have been intentionally excluded, as these would practically be identified by pre-estimation consistency tests. In addition, unlike the results in Table 10, the 200 scenarios in Table 11 are not only limited to noise but include variations in the location and magnitude of the bad data. For each of the four cases reported in Table 11, the row labeled with 1 corresponds to the LNR values for the first bad data point while the row marked with 2 is for the second point. The table reports the minimum, the maximum, and the average values of the normalized residuals over the 200 hundred scenarios, together with the percentage improvement that CEC offers as compared to CNE. In this case, the gain is substantial and exceeds 100% in some test instances.

Two points are worth mentioning before closing this section. First,

Appendix A

A.1. Complex zero injection measurements

Consider the complex zero injection power at node i and its conjugate:

$$s_i = 0 = u_i \bar{Y}_{ii} \bar{u}_i + u_i \sum_{k=1, k \neq i}^n \bar{Y}_{ik} \bar{u}_k$$

$$\bar{s}_i = 0 = \bar{u}_i Y_{ii} u_i + \bar{u}_i \sum_{k=1, k \neq i}^n Y_{ik} u_k$$

(33)

The corresponding elements of the Jacobian and conjugate Jacobian elements in J are:

dividing the actual weights by a scaling factor (as in Table 2) translates into dividing the actual normalized residuals by the square root of this scaling factor. The normalization is applied to both the CNE and CEC methods, and therefore, it does not affect the percentage improvement as reported in this subsection. Second, the effect of bad leverage points in the measurement set can be mitigated by using measurement weights modified by projection statistics [33,2].

7. Conclusion

This paper presented an algorithm for direct hybrid state estimation using a complex equality constrained normal equations approach. The complex variable formulation is advantageous for handling PMU measurements, and it is naturally suited for implementation on modern processors that allow fused multiply-accumulate operations and closely related advances. The use of equality constraints permit accurate modeling of zero injection measurements, and it has demonstrable benefits on the state estimator performance indices and bad data identification. The implementation of the CEC estimator is reported using the advanced vector extensions (AVX-2) set of instructions, which allows faster and specialized operations on complex numbers. Numerical results are reported on large scale transmission networks having different SCADA and PMU measurement configurations, and the results indicate that the AVX-2 implementation on networks with 9241 nodes requires less than 300 ms, thus conforming with real-time computing requirements. A comparison is carried out with two hybrid state estimation techniques: the complex normal equations (CNE) approach and the real equality constrained (REC) estimator; the comparative analysis shows that the proposed AVX-2 CEC implementation is superior to both methods in terms of solution speed and accuracy.

Declaration of Competing Interest

The authors declared that there is no conflict of interest.

$$\begin{aligned}\frac{\partial \bar{s}_i}{\partial u_i} &= \bar{Y}_{ii} \bar{u}_i + \sum_{k \neq i}^n \bar{Y}_{ik} \bar{u}_k \\ \frac{\partial \bar{s}_i}{\partial u_k} &= 0, \quad k \neq i \\ \frac{\partial \bar{s}_i}{\partial \bar{u}_i} &= \bar{Y}_{ii} u_i \\ \frac{\partial \bar{s}_i}{\partial \bar{u}_k} &= \bar{Y}_{ik} u_i, \quad k \neq i\end{aligned}\quad (34)$$

$$\begin{aligned}\frac{\partial \bar{s}_i}{\partial u_i} &= Y_{ii} \bar{u}_i = \left(\frac{\partial \bar{s}_i}{\partial \bar{u}_i} \right) \\ \frac{\partial \bar{s}_i}{\partial u_k} &= Y_{ik} \bar{u}_i = \left(\frac{\partial \bar{s}_i}{\partial \bar{u}_k} \right), \quad k \neq i \\ \frac{\partial \bar{s}_i}{\partial \bar{u}_i} &= Y_{ii} u_i + \sum_{k \neq i}^n Y_{ik} u_k = \left(\frac{\partial \bar{s}_i}{\partial u_i} \right) \\ \frac{\partial \bar{s}_i}{\partial \bar{u}_k} &= 0, \quad k \neq i\end{aligned}\quad (35)$$

A.2. Slack angle

The slack angle condition requires setting the imaginary part of the slack node voltage to zero:

$$u_s^{im} = \frac{i}{2}(\bar{u}_s - u_s) = 0 \quad (36)$$

The corresponding Jacobian and conjugate Jacobian elements in J are:

$$\frac{\partial u_s^{im}}{\partial u_s} = -\frac{i}{2} \quad (37)$$

$$\frac{\partial u_s^{im}}{\partial \bar{u}_s} = \frac{i}{2} = \left(\frac{\partial u_s^{im}}{\partial u_s} \right) \quad (38)$$

References

- [1] Nucera RR, Gilles ML. A blocked sparse matrix formulation for the solution of equality-constrained state estimation. *IEEE Trans Power Syst* 1991;6(1):214–24.
- [2] Abur A, Gómez Expósito A. Power system state estimation: theory and implementation. New York, NY: Marcel Dekker; 2004.
- [3] Gómez-Quiles C, Gil HA, de la Villa Jaén A, Gómez-Expósito A. Equality-constrained bilinear state estimation. *IEEE Trans Power Syst* 2013;28(2):902–10.
- [4] Taha AF, Qi J, Wang J, Panchal JH. Risk mitigation for dynamic state estimation against cyber attacks and unknown inputs. *IEEE Trans Smart Grid* 2018;9(2):886–99.
- [5] Borghetti A, Bottura R, Barbiroli M, Nucci CA. Synchrophasors-based distributed secondary voltage/var control via cellular network. *IEEE Trans Smart Grid* 2017;8(1):262–74.
- [6] Xu C, Abur A. A fast and robust linear state estimator for very large scale interconnected power grids. *IEEE Trans Smart Grid* 2018;9(5):4975–82.
- [7] Jin Z, Wall P, Chen Y, Yu J, Chakrabarti S, Terzija V. Analysis of hybrid state estimators: the effects of estimator formulations. *IEEE Trans Power Syst – Early Access*; 2018.
- [8] Zhou M, Centeno VA, Thorp JS, Phadke AG. An alternative for including phasor measurements in state estimators. *IEEE Trans Power Syst* 2006;21(4):1930–7.
- [9] Nuqui RF, Phadke AG. Hybrid linear state estimation utilizing synchronized phasor measurements. In: 2007 IEEE Lausanne Power Tech., Jul. 2007. p. 1665–9.
- [10] Cheng Y, Hu X, Gou B. A new state estimation using synchronized phasor measurements. In: 2008 IEEE international symposium on circuits and systems, May 2008. p. 2817–20.
- [11] Baltensperger R, Loosli A, Sauvain H, Zima M, Andersson G, Nuqui R. An implementation of two-stage hybrid state estimation with limited number of PMU. In: 10th IET international conference on Developments in Power System Protection (DPSP 2010), Mar. 2010. p. 1–5.
- [12] Sim oes Costa A, Albuquerque A, Bez D. An estimation fusion method for including phasor measurements into power system real-time modeling. *IEEE Trans Power Syst* 2013; 28(2):1910–20.
- [13] Wu T, Chung CY, Kamwa I. A fast state estimator for systems including limited number of PMUs. *IEEE Trans Power Syst* 2017;32(6):4329–39.
- [14] Bi T, Qin X, Yang Q. A novel hybrid state estimator for including synchronized phasor measurements. *Elect Power Syst Res* 2008;78(8):1343–52.
- [15] Chakrabarti S, Kyriakides E, Ledwich G, Ghosh A. Inclusion of PMU current phasor measurements in a power system state estimator. *IET Gener Transm Distrib* 2010;4(10):1104–15.
- [16] Valverde G, Chakrabarti S, Kyriakides E, Terzija V. A constrained formulation for hybrid state estimation. *IEEE Trans Power Syst* 2011;26(3):1102–9.
- [17] Chakhchoukh Y, Vittal V, Heydt GT, Ishii H. LTS-based robust hybrid SE integrating correlation. *IEEE Trans Power Syst* 2017;32(4):3127–35.
- [18] Korres GN, Manousakis NM. State estimation and bad data processing for systems including PMU and SCADA measurements. *Elect Power Syst Res* 2011;81(7):1514–24.
- [19] Murugesan V, Chakhchoukh Y, Vittal V, Heydt GT, Logic N, Sturgill S. PMU data buffering for power system state estimators. *IEEE Power Energy Tech Syst J* 2015;2(3):94–102.
- [20] Göl M, Abur A. A hybrid state estimator for systems with limited number of PMUs. *IEEE Trans Power Syst* 2015;30(3):1511–7.
- [21] Göl M. A decentralization method for hybrid state estimators. *IEEE Trans Power Syst* 2018;33(2):2070–7.
- [22] Džafić I, Jabr RA, Hrnjić T. Hybrid state estimation in complex variables. *IEEE Trans Power Syst* 2018;33(5):5288–96.
- [23] Hughes CJ. Single-instruction multiple-data execution. Morgan & Claypool; 2015. Available: <http://ieeexplore.ieee.org/xpl/articleDetails.jsp?arnumber=7123244>.
- [24] Lomont C. Introduction to Intel advanced vector extensions; 2011. <https://software.intel.com/en-us/articles/introduction-to-intel-advanced-vector-extensions> [accessed: 2018-06-3].
- [25] Wirtinger W. Zur formalen theorie der funktionen von mehr komplexen veränderlichen. *Mathematische Annalen* 1927;97:257–376.
- [26] Kreutz-Delgado K. The complex gradient operator and the CR-calculus; 2009. ArXiv e-prints, arXiv:0906.4835v1.
- [27] Jozs C, Fliscounakis S, Maeght J, Panciatici P. AC power flow data in MATPOWER and QCQP format: iTesla, RTE snapshots, and PEGASE; 2016, ArXiv e-prints, arXiv:1603.01533.
- [28] Džafić I, Jabr RA, Pal BC. Real-time equality-constrained hybrid state estimation in complex variables – test networks, <<https://www.dropbox.com/s/1p15itl2v43juw6/SETestNetworks.7z?dl=1>> [accessed: 2018-6-5].
- [29] Gómez-Expósito A, Abur A, Rousseaux P, de la Villa Jaén A, Gómez-Quiles C. On the use of PMUs in power system state estimation. In: 17th power systems computation conference, Aug. 2011. p. 1–13.
- [30] Venikov VA, Stroeve VA, Idelchick VI, Tarasov VI. Estimation of electrical power system steady-state stability in load flow calculations. *IEEE Trans Power Appar Syst* 1975;94(3):1034–41.
- [31] Ángelos EWS, Asada EN. Improving state estimation with real-time external equivalents. *IEEE Trans Power Syst* Mar. 2016;31(2):1289–96.
- [32] Do Coutto Filho MB, de Souza JCS, Ribeiro Guimaraens MA. Enhanced bad data processing by phasor-aided state estimation. *IEEE Trans Power Syst* 2014;29(5):2200–9.
- [33] Mili L, Cheniae MG, Vichare NS, Rousseeuw PJ. Robust state estimation based on projection statistics. *IEEE Trans Power Syst* 1996;11(2):1118–27.